

SpatialMosaic: A Multiview VLM Dataset for Partial Visibility

Kanghee Lee¹ Injae Lee¹ Minseok Kwak² Kwonyoung Ryu³ Jungi Hong¹ Jaesik Park¹
¹Seoul National University ²University College London ³POSTECH

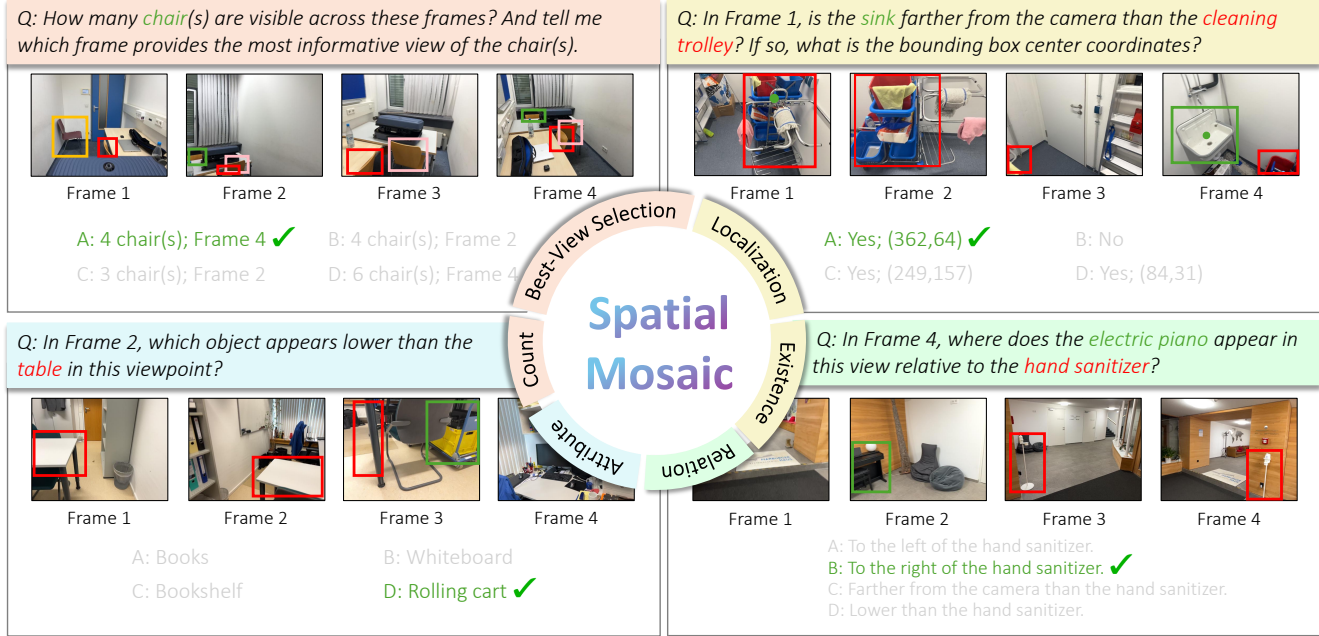


Figure 1. We present **SpatialMosaic**, a benchmark designed to evaluate 3D spatial reasoning capabilities from fragmented visual cues across multiple viewpoints. Our benchmark focuses on three challenging real-world scenarios involving partial visibility, occlusion, and low-overlap, where current MLLMs often struggle to maintain geometric and cross-view consistency.

Abstract

The rapid progress of Multimodal Large Language Models (MLLMs) has unlocked the potential for enhanced 3D scene understanding and spatial reasoning. However, existing approaches often rely on pre-constructed 3D representations or off-the-shelf reconstruction pipelines, which constrain scalability and real-world applicability. A recent line of work explores learning spatial reasoning directly from multi-view images, enabling Vision-Language Models (VLMs) to understand 3D scenes without explicit 3D reconstructions. Nevertheless, key challenges that frequently arise in real-world environments, such as partial visibility, occlusion, and low-overlap conditions that require spatial reasoning from fragmented visual cues, remain under-explored. To address these limitations, we propose a scalable multi-view data generation and annotation pipeline that constructs realistic

spatial reasoning QAs, resulting in **SpatialMosaic**, a comprehensive instruction-tuning dataset featuring 2M QA pairs. We further introduce **SpatialMosaic-Bench**, a challenging benchmark for evaluating multi-view spatial reasoning under realistic and challenging scenarios, consisting of 1M QA pairs across 6 tasks. In addition, we present **SpatialMosaicVLM**, a hybrid framework that integrates 3D reconstruction models as geometry encoders within VLMs for robust spatial reasoning. Extensive experiments demonstrate that our proposed dataset and VQA tasks effectively enhance spatial reasoning under challenging multi-view conditions, validating the effectiveness of our data generation pipeline in constructing realistic and diverse QA pairs. Code and dataset will be available soon.

1. Introduction

Spatial reasoning in 3D environments is a cornerstone of embodied intelligence, enabling agents to interpret complex scenes and interact effectively with the physical world. The recent progress of MLLMs [2, 22, 26, 49]) has raised the possibility of endowing them with human-level 3D spatial understanding, extending their success in 2D perception to more complex tasks such as object localization [13, 21, 44], depth estimation [37, 44, 50], metric distance prediction [9, 37, 44], and hierarchical holistic spatial reasoning capabilities [13, 37, 44]. However, existing approaches conventionally depend on pre-constructed 3D representations or off-the-shelf reconstruction modules [28, 40], which require costly data acquisition and limit scalability. Such reliance restricts their applicability in dynamic, real-world environments where pre-built 3D maps are impractical.

To address these limitations, recent studies [23, 24] have investigated deriving 3D spatial reasoning directly from multi-view images, thereby mitigating reliance on pre-constructed geometric priors or conventional 3D reconstruction pipelines. This paradigm not only alleviated such dependencies but also demonstrated superior performance in challenging 3D spatial reasoning tasks. However, existing works still fall short of capturing real-world conditions where available frames are sparse and contain limited overlapping visual information critical for spatial reasoning. In contrast, humans can integrate such partial observations across views to implicitly reconstruct coherent 3D scenes and reason about occluded objects that are not fully visible. Whether MLLMs can achieve comparable robustness under such imperfect conditions remains an open question. Building on these observations, we present fundamentally under-explored scenarios and constraints for 3D spatial reasoning in multi-view systems [29, 39, 47].

In this paper, we define three types of scenarios that each represent a unique spatial reasoning constraint. *Partial visibility* denotes a condition in multi-view settings where an object is visible only in a subset of views, instead of being observed from all camera viewpoints. *Occlusion* refers to a condition within a single view where the object is partially obscured by other instances or truncated by the camera's field of view. Lastly, *low-overlap* condition represents scenarios where the available views exhibit minimal cross-view overlap, providing limited information for spatial inference.

To handle these scenarios, we tackle this issue from both data and model perspectives. First, we propose a novel multi-view spatial data generation and annotation pipeline tailored to partial-visibility, occlusion, and low-overlap scenarios. With this pipeline, we construct *SpatialMosaic*, a comprehensive multi-view instruction-tuning dataset containing 2M QA pairs that capture challenging, frequently occurring real-world scenarios. Second, we introduce Spa-

Table 1. Multi-view spatial dataset comparison. Unlike existing datasets, *SpatialMosaic* focuses on challenging real-world scenarios with partial visibility, occlusion, and low-overlap conditions, providing a large-scale training set with diverse multi-view configurations (2–5 views) for robust spatial reasoning.

| Dataset | Split | | #Views | #Tasks | #Images | #QAs | | Open-sourced |
|-----------------------|-------|------|---------|--------|------------|-------|------|--------------|
| | Train | Eval | | | | Train | Eval | |
| <i>Video VLM</i> | | | | | | | | |
| VSI-Bench [38] | ✗ | ✓ | 8/16/32 | 8 | 288 videos | - | 5.1K | ✓ |
| VLM-3R [11] | ✓ | ✓ | 1–32 | 13 | - | 340K | 6.0K | ✓ |
| <i>Multi-view VLM</i> | | | | | | | | |
| BLINK [13] | ✗ | ✓ | 1–4 | 14 | 7.4K | - | 3.8K | ✓ |
| UniQA-3D [50] | ✗ | ✓ | 1–2 | 4 | 2.5K | - | 2.5K | ✗ |
| MultiSPA [37] | ✓ | ✓ | 1–5 | 26 | 1.1M | 27M | 7.8K | ✗ |
| SPAR [44] | ✓ | ✓ | 1–5 | 12 | 16.3M | 7M | 7.2K | ✓ |
| <i>SpatialMosaic</i> | ✓ | ✓ | 2–5 | 6 | 8M | 2M | 1M | ✓ |

tialMosaicVLM, a hybrid framework that leverages 3D reconstruction models as geometry encoders [19, 34–36] and unifies them with Vision-Language Models. Specifically, our approach encodes geometric cues into structured tokens and fuses them with per-view visual features, enabling the model to capture multi-view consistency and spatial context jointly. This design empowers the model to integrate observations across viewpoints and reason about spatial relationships in complex, real-world environments. In addition, we release *SpatialMosaic-Bench*, which provides a more comprehensive and challenging evaluation of spatial capabilities compared to existing multi-view benchmarks [13, 23, 43, 44]. It consists of 1M QA pairs across 6 tasks, focusing on spatial reasoning under realistic and challenging scenarios with up to 5 input views.

The key contributions are summarized as follows :

- We propose a scalable annotation framework applicable to existing multi-view datasets, enriching them with fine-grained visibility information to facilitate reasoning from fragmented visual observations across viewpoints.
- We present an automatic data generation pipeline that constructs spatial reasoning QAs under realistic and challenging multi-view conditions, resulting in *SpatialMosaic-Bench*, a comprehensive dataset for multi-view spatial reasoning.
- We introduce SpatialMosaicVLM, a hybrid framework combining 3D reconstruction models with VLM models to enable effective cross-view alignment and robust reasoning in realistic, multi-view environments.

2. Related Work

Spatial reasoning with MLLMs. Multimodal large language models (MLLMs) have demonstrated strong capabilities in open-world visual understanding, excelling at classification, segmentation, and captioning. Early models such

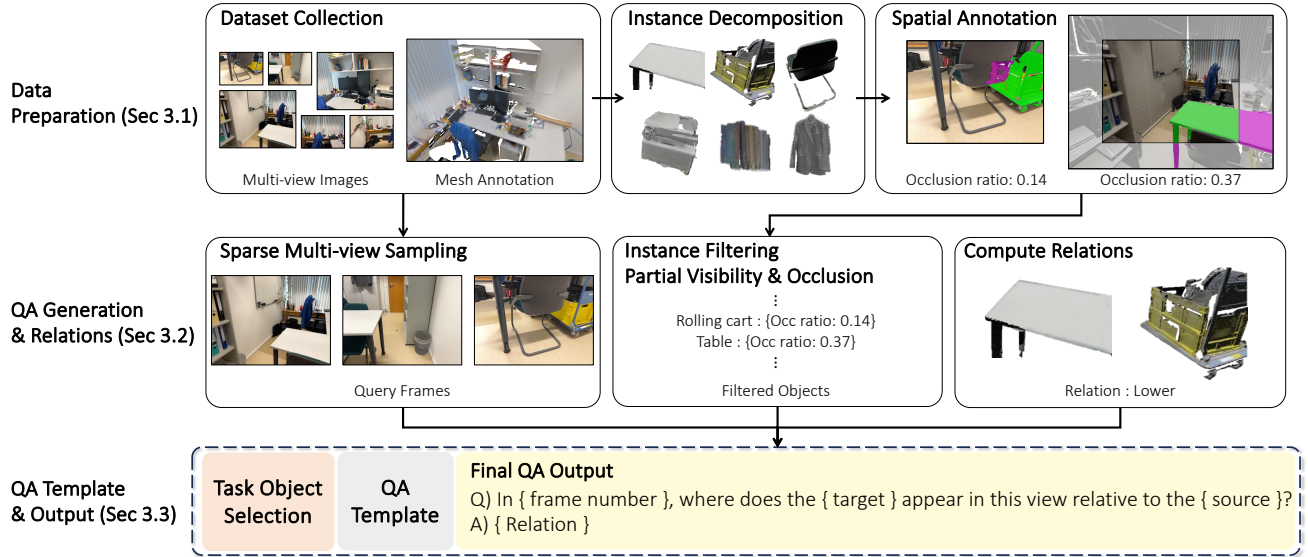


Figure 2. ***SpatialMosaic* data generation pipeline.** Given multi-view images dataset, with 3D annotations (Sec. 3.1), we compute object-level and image-level occlusion ratios for each instance. Images are then filtered by overlap to ensure diverse viewpoints, and instances are filtered based on visibility constraints (Sec. 3.2). Finally, spatial relations are computed and used to populate task-specific templates, generating geometrically grounded QA pairs (Sec. 3.3).

as Flamingo [2], BLIP-2 [22], MiniGPT-4 [49], and the LLaVA series [26] extend pretrained large language models (LLMs) with visual encoders, enabling instruction-following and open-ended reasoning on single-image inputs. More recent works seek to move beyond perception by explicitly modeling spatial relations, using datasets like NLVR2 [42], Neural Module Networks [3], and step-wise reasoning systems including ViperGPT [33] and Text2Scene [18]. Despite these advances, current MLLMs primarily focus on visible 2D cues, limiting their ability to reason when objects are partially visible or occluded in complex spatial configurations.

Towards 3D-aware Vision-Language Models. While 2D-based MLLMs have made progress in spatial reasoning, their reliance on single-view inputs limits the ability to capture full 3D scene structure. Recent approaches incorporate explicit 3D signals, extending vision-language models with depth maps, point clouds, or multi-view consistency. Models such as 3D-LLaVA [10], 3D-LLM [16], Grounded 3D-LLM [5], Scene-LLM [12], LSceneLLM [48] integrate 3D representations for tasks including visual question answering, grounding, and embodied navigation. Transformer-based methods like multi-view transformers for 3D grounding [17] align textual queries with 3D object locations, while benchmarks such as ScanQA [4], SQA3D [27], and ReferIt3D [1] measure performance in real-world settings. Nevertheless, current models remain challenged by cross-view inconsistencies, which degrade reasoning robustness in complex environments.

3D Reconstruction Models. Traditional 3D reconstruction

approaches, such as structure-from-motion [7, 15, 30, 31], multi-view stereo methods [14, 32], rely on sequential stages with feature extraction and matching, which provide time-consuming optimization. Recently, large-scale 3D reconstruction models learn generalizable geometric priors from massive multi-view data. Thanks to the rapid advancement of transformers, models such as DUS3R [36], MAST3R [19], CUT3R [35], and VGGT [34] provide 3D point maps with dense correspondences. These models operate over image patches or point tokens, coupled with differentiable geometric modules for epipolar reasoning, multi-view aggregation, or bundle-adjustment-style optimization, enabling robust generalization across scenes and domains. As a result, these models provide geometry-aware features that transfer across datasets and tasks. Building on this foundation, we integrate model patch tokens with 3D priors to strengthen multi-modal understanding in real-world spatial tasks. This integration improves cross-view consistency, stabilizes object identity under varying appearances, and enables robust reasoning under occlusion. We employ VGGT as a geometry encoder to ground the language model with spatial information by fusing CLIP encoder.

3. SpatialMosaic

While existing multi-view benchmarks [11, 37, 38, 44] provide VQA data for a variety of spatial reasoning tasks, they are typically limited to 2–3 multi-view images or sequential frames from video inputs. Moreover, they do not explicitly address challenges arising from partial visibility, occlusion,

and varying image overlap conditions that are pervasive in real-world environments. In practice, these are precisely the scenarios where current VLMs fail, struggling to integrate partial observations and low-overlap images into coherent spatial reasoning. To bridge this gap, we leverage the existing annotated scene dataset ScanNet++ [41], which provides high-quality RGB-D scans with dense 3D semantic annotations of real-world indoor scenes, making it ideal for creating challenging spatial reasoning benchmarks. We propose a scalable data generation framework that produces more than 3M QA pairs explicitly tailored to partial-visibility, occlusion, and low-overlap scenarios. Unlike prior benchmarks, our dataset includes a larger number of images with substantial perspective changes rather than sequential frames, yielding QA pairs that correspond to more realistic and challenging spatial reasoning tasks commonly encountered in real-world environments. Our data generation pipeline consists of three main stages, as illustrated in Fig. 2: (1) Data Preparation, (2) QA Generation and Relations, and (3) QA Template and Output.

3.1. Data Preparation

Object occlusion ratio. We introduce the object occlusion ratio to quantify the degree of occlusion for each instance. For each scene, ScanNet++ [41] provides annotated 3D point clouds $\mathcal{P} = \bigcup_{n=1}^N \mathcal{P}_n$, where \mathcal{P}_n represents the point cloud for instance n . We render the complete scene depth map \mathbf{D} and per-instance depth maps \mathbf{D}_n by projecting the provided 3D mesh onto each camera view using the corresponding camera parameters. Occluded and visible points for instance n are identified by comparing depth values at their projected locations. A point $\mathbf{p}_n \in \mathcal{P}_n$ is occluded when another object blocks the view ($\mathbf{D} < \mathbf{D}_n$), and visible otherwise:

$$\begin{aligned} \mathcal{O}_n &= \{\mathbf{p}_n \in \mathcal{P}_n \mid 0 < \mathbf{D} < \mathbf{D}_n\} \\ \mathcal{V}_n &= \{\mathbf{p}_n \in \mathcal{P}_n \mid \mathbf{D}_n \leq \mathbf{D}, \mathbf{D}_n < \infty\}. \end{aligned} \quad (1)$$

The object occlusion ratio is defined as:

$$r_{n,\text{obj}} = \frac{|\mathcal{O}_n|}{|\mathcal{O}_n| + |\mathcal{V}_n|} \quad (2)$$

where the object occlusion ratio $r_{n,\text{obj}} \in [0, 1]$ represents the proportion of occluded points for instance n , as illustrated in Fig. 3.

FoV occlusion ratio. In addition to object-level occlusion, instances may be partially occluded due to field of view (FoV) truncation, where parts of the object extend beyond the camera’s field of view. To quantify this, we introduce the FoV occlusion ratio, which measures the proportion of the instance truncated by the image boundary. As illustrated in Fig. 3, we create an extended field of view reference image with doubled resolution $2H \times 2W$ centered around the original view by shifting the principal point to the center

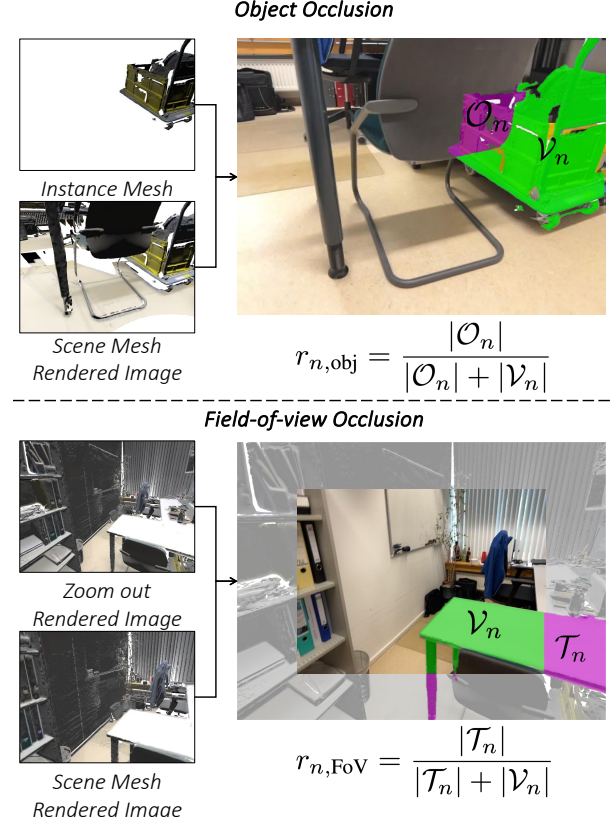


Figure 3. **Occlusion ratio calculation.** We render each instance independently to measure visible (green) and occluded (magenta) pixels. **Object Occlusion:** Object-level occlusion (r_{obj}) captures inter-object obstruction from the actual camera view. **Field-of-view Occlusion:** Field-of-view truncation (r_{FoV}) uses extended field-of-view rendering to quantify boundary occlusion from frame cropping.

of the extended field. The extended intrinsic matrix $\tilde{\mathbf{K}}$ is defined as:

$$\tilde{\mathbf{K}} = \begin{bmatrix} f_x & 0 & c_x + W/2 \\ 0 & f_y & c_y + H/2 \\ 0 & 0 & 1 \end{bmatrix} \quad (3)$$

where f_x, f_y are the focal lengths and c_x, c_y are the principal point coordinates from the original intrinsic matrix \mathbf{K} . Using this extended intrinsic matrix, we project each point to obtain (\tilde{u}, \tilde{v}) in the extended image coordinate system. We then render both the instance depth map $\tilde{\mathbf{D}}_n$ and the complete scene depth map $\tilde{\mathbf{D}}$ in this extended view.

We define the visible point sets within the original FoV region \mathcal{R} and the FoV-truncated region \mathcal{T}_n as follows:

$$\begin{aligned} \mathcal{V}_n &= \{\mathbf{p}_n \in \mathcal{P}_n \mid 0 < \tilde{\mathbf{D}}_n \leq \tilde{\mathbf{D}} < \infty, (\tilde{u}, \tilde{v}) \in \mathcal{R}\} \\ \mathcal{T}_n &= \{\mathbf{p}_n \in \mathcal{P}_n \mid 0 < \tilde{\mathbf{D}}_n \leq \tilde{\mathbf{D}} < \infty, (\tilde{u}, \tilde{v}) \in \tilde{\mathcal{R}} \setminus \mathcal{R}\} \end{aligned} \quad (4)$$

where $\mathcal{R} = [W/2, 3W/2] \times [H/2, 3H/2]$ represents the original FoV region and $\tilde{\mathcal{R}} = [0, 2W) \times [0, 2H)$ represents the extended canvas region. The FoV occlusion ratio is then defined as:

$$r_{n,\text{FoV}} = \frac{|\mathcal{T}_n|}{|\mathcal{T}_n| + |\mathcal{V}_n|} \quad (5)$$

where $r_{n,\text{FoV}} \in [0, 1]$ quantifies the proportion of points truncated by the FoV boundaries, with $r_{n,\text{FoV}} = 0$ indicating the instance is fully within the original field of view.

3.2. QA Generation and Relations

Sparse Multi-view Sampling. To construct multi-frame spatial reasoning tasks, we sample image pairs with limited overlap to encourage integration of diverse viewpoints. For each scene, we compute the overlap ratio between i, j th images by measuring the intersection-over-union of their visible 3D points. The overlap ratio is defined as follows,

$$\text{Overlap}(i, j) = \frac{|\mathcal{V}^i \cap \mathcal{V}^j|}{|\mathcal{V}^i \cup \mathcal{V}^j|}, \quad \mathcal{V} = \bigcup_{n=1}^N \mathcal{V}_n. \quad (6)$$

We retain only image pairs with overlap ratios below 30%, thereby filtering out redundant images with excessive shared content. This constraint encourages integrative spatial reasoning across sparse and diverse viewpoints rather than simple matching of overlapping regions.

Accurate overlap estimation, however, requires precise scene geometry. Although datasets such as ScanNet [8] provide RGB-D scans and 3D reconstructions, their meshes often suffer from noise and incompleteness, which hinder reliable overlap computation. To enable accurate overlap computation for view sampling, we leverage the high-quality meshes provided by ScanNet++ [41], which offers dense and accurate geometric annotations crucial for precise overlap estimation.

Instance Filtering. Not all instances are suitable for generating meaningful QA pairs. We filter instances based on two criteria: (1) the target instance must not appear in all images within the selected combination to ensure partial visibility, and (2) the target instance must have an occlusion ratio below 0.9 in at least one image (objects with occlusion ratios above 0.9 are nearly impossible for humans to observe). Additionally, there are task-specific filtering criteria such as selecting objects as target instances only if it is above the minimum occlusion threshold (e.g., above 0.4), and ensuring that the source instance is visible while the target instance is not visible in the selected query image. Collectively, these constraints substantially elevate the spatial complexity of the generated QAs; they reduce reliance on redundant visibility cues, force models to reason under minimal information with asymmetric view conditions, and require accurate spatial inference even when object instances exhibit no correlation under a single image. As a result, our

Table 2. Task definitions and one-shot examples in *Spatial-Mosaic*.

| Task | One-shot examples |
|-------------------------------------------------|----------------------------------------------------------------------------------------------------------------------------------------------------------------------|
| Object Count (4-option MCA) | Question: How many chairs are visible across these frames? Answer: There are 3 chairs. |
| Best-View Selection (4-option MCA) | Question: Which frame provides the most informative view of the table? Answer: Frame 2 |
| Object Localization (4-option MCA) | Question: Is there a monitor in Frame 1? If so, what is the bounding box center coordinates? Answer: Yes; (512, 384). |
| Occlusion-Aware Object Existence (binary) | Question: In Frame 3, is the mouse appears farther from the camera than the laptop in this viewpoint? Answer: Yes. |
| Occlusion-Aware Attribute (4-option MCA) | Question: In Frame 2, which object appears lower than the able in this viewpoint? Answer: Rolling cart. |
| Occlusion-Aware Spatial Relation (4-option MCA) | Question: In Frame 4, where does the electric piano appear in this view relative to the hand sanitizer? Answer: To the right of the hand sanitizer. |

QA set captures challenging real-world visibility patterns that conventional datasets fail to represent.

Compute Relations. For spatial-relation tasks, we extract each object’s 3D oriented bounding box and integrate it with camera coordinates to compute positional relationships along the X, Y, and Z axes in the specified image. These relationships define the underlying reasoning context, allowing us to determine directional relations (e.g., “to the left side, above”) between object pairs. The computed relations serve as ground-truth labels for spatial reasoning questions.

3.3. QA Template and Output

Task and Object Selection. Based on the filtered instances and computed relations from the previous stage, we select appropriate source and target objects for each task type. The selection process considers task requirements and ensures that selected objects satisfy visibility and occlusion constraints established in earlier stages.

QA Template Generation. We define templates for 6 task categories using template-based generation, where placeholders such as [source_obj], [target_obj], or [relation] are replaced with concrete object labels and computed spatial information. The tasks include: Object Count, Best-View Selection, Object Localization, Occlusion-Aware Object Existence, Occlusion-Aware Attribute, and Occlusion-Aware Spatial Relation. Table 2 and Fig. 1 illustrate representative examples for each task category.

Answer options are generated automatically according to the predefined QA format: binary questions contain one correct and one inverted relation, while four-option multiple-choice questions include one correct answer and three distractor relations with incorrect spatial configurations. Specif-

ically for four-option multiple-choice questions, one distractor relation corresponds to the direct opposite of the true relation, while the remaining two are chosen by calculating the ground-truth relation such that the distractors represent orthogonal opposite relations. Using this method, there can always be only one correct relation among the answer choices, as the remaining three are always spatially inconsistent with the true relation. For example, if the target instance is positioned above, in front of, and to the right of the source instance, and the correct answer is "right", the distractors become "left", "behind", and "below." The ground-truth label is calculated in accordance with the relation or image, consistent with the 3D metadata and visibility constraints. For counting-based tasks, we track instance IDs across frames to ensure identical objects from different viewpoints are counted only once. Additional QA templates and detailed generation pipelines are provided in the Appendix.

3.4. SpatialMosaic Benchmark

SpatialMosaic-Bench is a large-scale multi-view benchmark explicitly designed to evaluate spatial reasoning under occlusion and partial visibility. The benchmark comprises 2M QA pairs across 6 task categories derived from real-world indoor scenes in ScanNet++ [41].

Evaluation protocol. Each QA instance consists of 2-5 frames, a question, and multiple answer options. Models select one option, and performance is measured by accuracy against ground-truth answers. To enable fine-grained analysis, we annotate every QA with two diagnostic scenarios: (1) *Visibility Scenario* indicates whether target objects are consistently visible or partially occluded across frames, and (2) *GT Scenario* indicates whether all instances of the target category in the scene are captured or only a subset is visible. Together, these axes support structured performance breakdowns across a continuum of difficulty levels. In particular, the combination *Partially Visible + Partial Coverage* corresponds to the most challenging regime, where models must aggregate sparse cues, resolve viewpoint inconsistencies, and reason over incomplete category-level information. This diagnostic framework enables us to analyze not only overall accuracy but also the specific multi-view conditions under which models succeed or fail. Additional evaluation details are provided in the Appendix.

4. SpatialMosaicVLM Architecture

We integrate VGGT [34], a 3D reconstruction model, into our VLM architecture as a spatial encoder. VGGT [34] provides geometry-aware token representations that are fused with per-view visual tokens from the image encoder. This joint representation captures multi-view consistency while maintaining geometric structure, thereby supporting spatial reasoning across viewpoints.

To leverage this joint representation, we extract and fuse

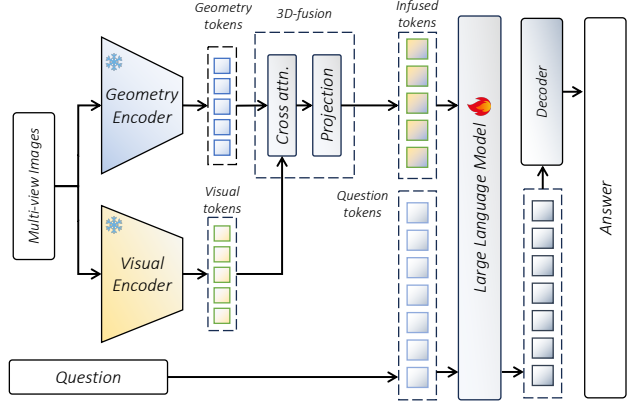


Figure 4. **SpatialMosaicVLM architecture.** Multi-image inputs are processed through parallel Geometry and Visual Encoders to extract 3D structural and appearance features. The resulting geometry and visual tokens are fused via cross-attention, then combined with question tokens and processed by a Large Language Model to answer spatial reasoning questions under occlusion and partial visibility circumstances.

visual and geometric tokens from both the encoder and decoder stages as illustrated in Fig. 4. Specifically, each image \mathbf{I} passes through both the visual encoder E_{vis} and geometric encoder E_{geo} to obtain visual tokens F_{vis} and geometric tokens F_{geo} , respectively:

$$F_{vis} = E_{vis}(\mathbf{I}), \quad F_{geo} = E_{geo}(\mathbf{I}). \quad (7)$$

We then fuse the visual tokens F_{vis} with geometric tokens F_{geo} via cross-attention to obtain 3D aware visual tokens :

$$F_{fuse} = \sigma \left(\frac{(F_{vis} W_q)(F_{geo} W_k)^T}{\sqrt{d_k}} \right) (F_{geo} W_v) \quad (8)$$

where W_q, W_k, W_v are learnable projection matrices, d_k is the key dimension and σ is softmax operation. Following LLaVA-Next-Video [46], the fused tokens F_{fuse} pass through a two-layer projector to obtain F'_{fuse} , which are concatenated with question tokens $F_{question}$ as input to the language model backbone.

5. Experiments

We evaluate our approach across two complementary settings, each examining a distinct aspect of multi-view spatial reasoning. First, we analyze model performance on *SpatialMosaic-Bench* (Sec. 5.1), which assesses robustness under partial visibility, occlusion, and low-overlap conditions. Next, we examine zero-shot transfer to temporal spatial reasoning tasks on VSTI-Bench [11] (Sec. 5.2), where models are expected to handle camera-centric and numerical queries never seen during training. Together, these evaluations provide a comprehensive view of both in-domain effectiveness and out-of-domain generalization.

Table 3. Quantitative results on *SpatialMosaic-Bench* across six spatial reasoning tasks. **Bold** and underline indicate the best and second-best performance within open-sourced VLMs for each task, respectively. **Highlighting** denotes the top-3 ranked models overall. * denotes models trained on VSTI-Bench [11].

| Methods | Rank | Avg. | Obj. Count | Best View. | Obj. Exist. | Obj. Att. | Obj. Rel. | Obj. Loc. |
|--------------------------|------|-------------|-------------|-------------|-------------|-------------|-------------|------------|
| <i>Open-sourced VLMs</i> | | | | | | | | |
| LLaVA-OneVision-0.5B | 11 | 37.7 | 29.5 | 44.4 | 55.3 | 20.7 | 37.7 | 38.3 |
| InternVL2-2B | 8 | 39.9 | 65.8 | 49.4 | 47.8 | 26.4 | 34.8 | 53.1 |
| LLaVA-NeXT-Video-7B | 5 | 47.8 | 61.1 | 41.0 | 45.7 | 34.2 | 54.6 | 37.2 |
| LLaVA-OneVision-7B | 7 | 42.8 | 58.5 | 37.5 | 56.1 | 32.6 | 37.9 | 37.8 |
| LongVA-7B | 10 | 38.2 | 34.5 | 27.5 | 57.4 | 24.2 | 42.4 | 26.2 |
| InternVL2-8B | 6 | 46.0 | 61.6 | 49.0 | 54.4 | 38.6 | 39.8 | 43.3 |
| VILA-1.5-8B | 9 | 38.7 | 40.2 | 24.7 | 52.5 | 32.5 | 37.5 | 32.4 |
| VILA-1.5-40B | 4 | 48.5 | 56 | 50.7 | 58.9 | 31.6 | 54.2 | 40.6 |
| VLM-3R* (7B) | 3 | 49.3 | 51.9 | 36.6 | 61.4 | 42.2 | 51.4 | 38.3 |
| VLM-3R (7B) | 2 | <u>81.7</u> | <u>89.8</u> | 73.0 | <u>81.2</u> | <u>74.2</u> | <u>83.6</u> | 100 |
| SpatialMosaicVLM (7B) | 1 | 81.8 | 89.9 | <u>72.9</u> | 81.5 | 74.3 | 84.0 | 100 |

Baselines. Following prior efforts in spatial reasoning, we evaluate our method against a suite of open-sourced Video-Language Models, which serve as our baselines under identical multi-view input protocols. The comparing models include LLaVA-OneVision-0.5B [20], InternVL2-2B [6], LLaVA-NeXT-Video-7B [46], LLaVA-OneVision-7B [20], LongVA-7B [45], InternVL2-8B [6], VILA-1.5-8B [25], and VILA-1.5-40B [25]. All baselines receive the same set of multi-view frames at a resolution of 518×518 per view, ensuring consistent evaluation across architectures. Model outputs are derived using their default decoding settings without task-specific tuning.

Datasets. We evaluate our proposed method across two spatial benchmarks designed to measure multi-view spatial understanding and scene reasoning. Our evaluation covers diverse task categories, including object-level geometry reasoning, view-consistent spatial relation inference, and temporal dynamics estimation. First, we perform evaluation on VSTI-Bench [11], which extends VSI-Bench [38] evaluation to temporal settings by focusing on reasoning about spatial configurations evolving over time. These include object displacement, camera-object distance changes, relative positional shifts, and camera motion direction. The benchmark emphasizes long-range temporal aggregation and evaluates whether models can maintain coherent spatial representation across time. *SpatialMosaic-Bench* introduced in this work, offers a more challenging evaluation protocol by constructing view sets with deliberately minimal geometric redundancy. This benchmark is designed to probe robustness under incomplete spatial evidence and to reflect more realistic low-overlap conditions.

Implementation Details. For training VLM-3R [11] and SpatialMosaicVLM, we employ 8 NVIDIA H200 GPUs with a batch size of 4. We used accelerator library with Deep-

Speed ZeRO stage 2 optimization for distributed training. The learning rate is set to 2×10^{-5} , the weight decay to 0.0, and we adopt a cosine learning rate scheduler. Training is performed for 5 epochs. Both the visual and geometry encoders are frozen, and multi-view features are integrated through a 3D-fusion module composed of a cross-attention layer followed by a projection layer.

5.1. Evaluation on SpatialMosaic-Bench

SpatialMosaic-Bench provides a challenging and realistic evaluation environment characterized by partial visibility, occlusion, and minimal overlap across viewpoints. These conditions limit geometric redundancy and require models to infer spatial structure from fragmented observations rather than relying on stable cross-frame correspondences. To assess whether existing models can integrate such incomplete visual cues, we first evaluate strong MLLM baselines that demonstrate robust spatial reasoning in conventional image or video settings. Despite their capabilities, these models struggle to maintain consistency under occlusion-heavy and low-overlap conditions. They frequently misinterpret object presence, misidentify spatial relations, or fail to localize objects across sparsely aligned viewpoints. This reveals the limitations of current approaches when visual evidence across views is limited or only partially observed. Next, to validate the effectiveness of our instruction tuning dataset and realistic VQA tasks, we fine-tune both VLM-3R and our model on *SpatialMosaic* and evaluate them on *SpatialMosaic-Bench*. As shown in Table 3, both models demonstrate strong capability to integrate partial observations across views, yielding substantial improvements over strong MLLM baselines. Notably, our model outperforms LLaVA-NeXT-Video-7B [46] by 34%, underscoring the importance of training models under the challenging conditions

Table 4. Quantitative results on VSTI-Bench [11] across five temporal reasoning tasks. **Bold** and underline indicate the best and second-best performance within open-sourced VLMs for each task, respectively. **Highlighting** denotes the top-3 ranked models overall. \dagger denotes models trained on *SpatialMosaic*.

| Methods | Rank | Avg. | Cam-Obj Abs. Dist. | Cam. Displace. | Cam. Mov. Dir. | Obj-Obj Rel. Pos. | Cam-Obj Rel. Dist. |
|---------------------------------|----------|-------------|-----------------------|-------------------|-------------------|----------------------|-----------------------|
| <i>Proprietary Models (API)</i> | | | | | | | |
| GPT-4o | 7 | 38.2 | 29.5 | 23.4 | 37.3 | 58.1 | 42.5 |
| Gemini-1.5 Flash | 13 | 32.1 | 28.5 | 20.9 | 24.4 | 52.6 | 33.9 |
| <i>Open-sourced VLMs</i> | | | | | | | |
| LLaVA-OneVision-0.5B | 11 | 36.9 | 16.5 | 32.4 | 46.1 | 50.5 | 39.0 |
| InternVL2-2B | 9 | 38.1 | 17.7 | <u>27.8</u> | 43.0 | 54.9 | 47.2 |
| LLaVA-NeXT-Video-7B | 6 | 40.0 | 28.2 | 1.8 | 49.8 | 64.7 | 55.6 |
| LLaVA-OneVision-7B | 5 | 41.7 | 29.9 | 19.3 | 47.5 | 62.1 | 49.8 |
| LongVA-7B | 12 | 32.3 | 13.5 | 5.1 | 43.7 | 57.9 | 41.2 |
| InternVL2-8B | 4 | 43.5 | 32.9 | 13.5 | 48.0 | 68.0 | <u>55.0</u> |
| VILA-1.5-8B | 10 | 37.3 | 30.1 | 27.3 | 42.2 | 50.4 | 36.7 |
| VILA-1.5-40B | 7 | 38.2 | 28.2 | 15.7 | 28.8 | 65.4 | 53.0 |
| LLaVA-NeXT-Video-72B | 3 | 44.0 | <u>32.3</u> | 10.5 | 48.1 | 78.3 | 50.9 |
| VLM-3R \dagger (7B) | 2 | <u>46.7</u> | 28.6 | 7.1 | 47.9 | 73.9 | 53.0 |
| SpatialMosaicVLM (7B) | 1 | 46.8 | 27.8 | 5.0 | <u>48.2</u> | <u>74.2</u> | 52.3 |

outlined in this work. Additionally, we assess whether instruction tuning on VSTI-Bench [11] offers meaningful zero-shot generalization capability to our benchmark. Although VSTI-Bench is designed for temporal spatial reasoning, we find that models tuned on VSTI-Bench do not achieve a notable performance advantage over existing MLLMs baselines [6, 25, 46] when evaluated on *SpatialMosaic-Bench*. This result indicates that the supervision provided by VSTI-Bench does not sufficiently capture the challenges posed by partial visibility, occlusion, and low-overlap conditions. It further highlights the necessity of dedicated instruction-tuning datasets tailored to multi-view spatial reasoning, such as the one introduced in this work.

5.2. Evaluation on VSTI-Bench

We further evaluate whether training on our challenging *SpatialMosaic* dataset enables models to generalize to unseen multi-view spatial reasoning tasks and benchmarks. To this end, we perform zero-shot evaluation on VSTI-Bench [11] by directly applying both VLM-3R [11] and SpatialMosaicVLM without any additional fine-tuning. Notably, *SpatialMosaic* does not contain camera-centric tasks such as displacement or movement direction, nor numerical question types like absolute camera-object distance. During training, models encountered only multiple-choice spatial reasoning questions and never saw such task categories or question types from VSTI-Bench [11]. Even under this strict zero-shot setup, both VLM-3R [11] and SpatialMosaicVLM outperform all MLLM baselines, showing strong zero-shot capability in multi-view spatial reasoning. In par-

ticular, SpatialMosaicVLM even surpasses LLaVA-Next-Video-72B [46], which has more than ten times the number of parameters. These results demonstrate that training under realistic multi-view conditions, including partial visibility and heavy occlusion, enables models to develop spatial reasoning capabilities that generalize well to unseen scenarios.

6. Conclusion

In this work, we take an initial step toward tackling the challenges of partial visibility, occlusion, and low-overlap conditions in settings that require models to integrate fragmented visual cues to form coherent 3D understanding. To support this goal, we introduced a scalable spatial annotation framework and an automatic multi-view data generation pipeline, enabling the construction of *SpatialMosaic* and *SpatialMosaic-Bench*, which capture realistic and challenging multi-view scenarios. We further proposed SpatialMosaicVLM, a hybrid framework that combines geometric cues from 3D reconstruction models to enable effective cross-view alignment and robust spatial reasoning. Experiments demonstrate that instruction-tuning on our dataset improves performance under incomplete visual evidence and yields strong zero-shot generalization to existing multi-view spatial benchmark. These results highlight the importance of equipping models with the ability to aggregate partial observations and infer coherent 3D structure from limited cues. We believe that this work enhances the scalability and real-world applicability of MLLMs, contributing to narrowing the gap toward human-level multi-view reasoning.

References

[1] Panos Achlioptas, Ahmed Abdelreheem, Fei Xia, Mohamed Elhoseiny, and Leonidas Guibas. Referit3d: Neural listeners for fine-grained 3d object identification in real-world scenes. In *European conference on computer vision*, pages 422–440. Springer, 2020. 3

[2] Jean-Baptiste Alayrac, Jeff Donahue, Pauline Luc, Antoine Miech, Iain Barr, Yana Hasson, Karel Lenc, Arthur Mensch, Katherine Millican, Malcolm Reynolds, et al. Flamingo: a visual language model for few-shot learning. *Advances in neural information processing systems*, 35:23716–23736, 2022. 2, 3

[3] Jacob Andreas, Marcus Rohrbach, Trevor Darrell, and Dan Klein. Neural module networks. In *Proceedings of the IEEE conference on computer vision and pattern recognition*, pages 39–48, 2016. 3

[4] Daichi Azuma, Taiki Miyanishi, Shuhei Kurita, and Motoaki Kawanabe. Scanqa: 3d question answering for spatial scene understanding. In *proceedings of the IEEE/CVF conference on computer vision and pattern recognition*, pages 19129–19139, 2022. 3

[5] Yilun Chen, Shuai Yang, Haifeng Huang, Tai Wang, Runsen Xu, Ruiyuan Lyu, Duhua Lin, and Jiangmiao Pang. Grounded 3d-llm with referent tokens. *arXiv preprint arXiv:2405.10370*, 2024. 3

[6] Zhe Chen, Weiyun Wang, Hao Tian, Shenglong Ye, Zhangwei Gao, Erfei Cui, Wenwen Tong, Kongzhi Hu, Jiapeng Luo, Zheng Ma, et al. How far are we to gpt-4v? closing the gap to commercial multimodal models with open-source suites. *Science China Information Sciences*, 67(12):220101, 2024. 7, 8, 1

[7] Hainan Cui, Xiang Gao, Shuhan Shen, and Zhanyi Hu. Hsfp: Hybrid structure-from-motion. 2017. 3

[8] Angela Dai, Angel X Chang, Manolis Savva, Maciej Halber, Thomas Funkhouser, and Matthias Nießner. Scannet: Richly-annotated 3d reconstructions of indoor scenes. In *Proceedings of the IEEE conference on computer vision and pattern recognition*, pages 5828–5839, 2017. 5

[9] Erik Daxberger, Nina Wenzel, David Griffiths, Haiming Gang, Justin Lazarow, Gefen Kohavi, Kai Kang, Marcin Eichner, Yinfei Yang, Afshin Dehghan, et al. Mm-spatial: Exploring 3d spatial understanding in multimodal llms. In *Proceedings of the IEEE/CVF International Conference on Computer Vision*, pages 7395–7408, 2025. 2

[10] Jiajun Deng, Tianyu He, Li Jiang, Tianyu Wang, Feras Dayoub, and Ian Reid. 3d-llava: Towards generalist 3d llms with omni superpoint transformer. In *Proceedings of the Computer Vision and Pattern Recognition Conference*, pages 3772–3782, 2025. 3

[11] Zhiwen Fan, Jian Zhang, Renjie Li, Junge Zhang, Runjin Chen, Hezhen Hu, Kevin Wang, Huazhi Qu, Dilin Wang, Zhicheng Yan, et al. Vlm-3r: Vision-language models augmented with instruction-aligned 3d reconstruction. *arXiv preprint arXiv:2505.20279*, 2025. 2, 3, 6, 7, 8

[12] Rao Fu, Jingyu Liu, Xilun Chen, Yixin Nie, and Wenhui Xiong. Scene-llm: Extending language model for 3d visual understanding and reasoning. *arXiv preprint arXiv:2403.11401*, 2024. 3

[13] Xingyu Fu, Yushi Hu, Bangzheng Li, Yu Feng, Haoyu Wang, Xudong Lin, Dan Roth, Noah A Smith, Wei-Chiu Ma, and Ranjay Krishna. Blink: Multimodal large language models can see but not perceive. In *European Conference on Computer Vision*, pages 148–166. Springer, 2024. 2

[14] Yasutaka Furukawa, Carlos Hernández, et al. Multi-view stereo: A tutorial. *Foundations and trends® in Computer Graphics and Vision*, 9(1-2):1–148, 2015. 3

[15] Richard Hartley and Andrew Zisserman. *Multiple view geometry in computer vision*. Cambridge university press, 2003. 3

[16] Yining Hong, Haoyu Zhen, Peihao Chen, Shuhong Zheng, Yilun Du, Zhenfang Chen, and Chuang Gan. 3d-llm: Injecting the 3d world into large language models. *Advances in Neural Information Processing Systems*, 36:20482–20494, 2023. 3

[17] Shijia Huang, Yilun Chen, Jiaya Jia, and Liwei Wang. Multi-view transformer for 3d visual grounding. In *Proceedings of the IEEE/CVF Conference on Computer Vision and Pattern Recognition*, pages 15524–15533, 2022. 3

[18] Inwoo Hwang, Hyeonwoo Kim, and Young Min Kim. Text2scene: Text-driven indoor scene stylization with part-aware details. In *Proceedings of the ieee/cvf conference on computer vision and pattern recognition*, pages 1890–1899, 2023. 3

[19] Vincent Leroy, Yohann Cabon, and Jérôme Revaud. Grounding image matching in 3d with mast3r. In *European Conference on Computer Vision*, pages 71–91. Springer, 2024. 2, 3

[20] Bo Li, Yuanhan Zhang, Dong Guo, Renrui Zhang, Feng Li, Hao Zhang, Kaichen Zhang, Peiyuan Zhang, Yanwei Li, Ziwei Liu, et al. Llava-onevision: Easy visual task transfer. *arXiv preprint arXiv:2408.03326*, 2024. 7

[21] Dingming Li, Hongxing Li, Zixuan Wang, Yuchen Yan, Hang Zhang, Siqi Chen, Guiyang Hou, Shengpei Jiang, Wensi Zhang, Yongliang Shen, et al. Viewspatial-bench: Evaluating multi-perspective spatial localization in vision-language models. *arXiv preprint arXiv:2505.21500*, 2025. 2

[22] Junnan Li, Dongxu Li, Silvio Savarese, and Steven Hoi. Blip-2: Bootstrapping language-image pre-training with frozen image encoders and large language models. In *International conference on machine learning*, pages 19730–19742. PMLR, 2023. 2, 3

[23] Kunchang Li, Yali Wang, Yinan He, Yizhuo Li, Yi Wang, Yi Liu, Zun Wang, Jilan Xu, Guo Chen, Ping Luo, et al. Mvbench: A comprehensive multi-modal video understanding benchmark. In *Proceedings of the IEEE/CVF Conference on Computer Vision and Pattern Recognition*, pages 22195–22206, 2024. 2

[24] Yiming Li, Zhiding Yu, Christopher Choy, Chaowei Xiao, Jose M Alvarez, Sanja Fidler, Chen Feng, and Anima Anandkumar. Voxformer: Sparse voxel transformer for camera-based 3d semantic scene completion. In *Proceedings of the IEEE/CVF conference on computer vision and pattern recognition*, pages 9087–9098, 2023. 2

[25] Ji Lin, Hongxu Yin, Wei Ping, Pavlo Molchanov, Mohammad Shoeybi, and Song Han. Vila: On pre-training for visual

language models. In *Proceedings of the IEEE/CVF conference on computer vision and pattern recognition*, pages 26689–26699, 2024. 7, 8

[26] Haotian Liu, Chunyuan Li, Qingyang Wu, and Yong Jae Lee. Visual instruction tuning. *Advances in neural information processing systems*, 36:34892–34916, 2023. 2, 3

[27] Xiaojian Ma, Silong Yong, Zilong Zheng, Qing Li, Yitao Liang, Song-Chun Zhu, and Siyuan Huang. Sq3d: Situated question answering in 3d scenes. *arXiv preprint arXiv:2210.07474*, 2022. 3

[28] Ricardo Martin-Brualla, Noha Radwan, Mehdi SM Sajjadi, Jonathan T Barron, Alexey Dosovitskiy, and Daniel Duckworth. Nerf in the wild: Neural radiance fields for unconstrained photo collections. In *Proceedings of the IEEE/CVF conference on computer vision and pattern recognition*, pages 7210–7219, 2021. 2

[29] Muhammad Ferjad Naeem, Muhammad Gul Zain Ali Khan, Yongqin Xian, Muhammad Zeshan Afzal, Didier Stricker, Luc Van Gool, and Federico Tombari. I2mvformer: Large language model generated multi-view document supervision for zero-shot image classification. In *Proceedings of the IEEE/CVF Conference on Computer Vision and Pattern Recognition*, pages 15169–15179, 2023. 2

[30] Linfei Pan, Dániel Baráth, Marc Pollefeys, and Johannes L Schönberger. Global structure-from-motion revisited. In *European Conference on Computer Vision*, pages 58–77. Springer, 2024. 3

[31] Johannes L Schönberger and Jan-Michael Frahm. Structure-from-motion revisited. In *Proceedings of the IEEE conference on computer vision and pattern recognition*, pages 4104–4113, 2016. 3

[32] Johannes L Schönberger, Enliang Zheng, Jan-Michael Frahm, and Marc Pollefeys. Pixelwise view selection for unstructured multi-view stereo. In *Computer Vision–ECCV 2016: 14th European Conference, Amsterdam, The Netherlands, October 11–14, 2016, Proceedings, Part III 14*, pages 501–518. Springer, 2016. 3

[33] Dídac Surís, Sachit Menon, and Carl Vondrick. Vipergrpt: Visual inference via python execution for reasoning. In *Proceedings of the IEEE/CVF international conference on computer vision*, pages 11888–11898, 2023. 3

[34] Jianyuan Wang, Minghao Chen, Nikita Karaev, Andrea Vedaldi, Christian Rupprecht, and David Novotny. Vggt: Visual geometry grounded transformer. In *Proceedings of the Computer Vision and Pattern Recognition Conference*, pages 5294–5306, 2025. 2, 3, 6

[35] Qianqian Wang, Yifei Zhang, Aleksander Holynski, Alexei A Efros, and Angjoo Kanazawa. Continuous 3d perception model with persistent state. In *Proceedings of the Computer Vision and Pattern Recognition Conference*, pages 10510–10522, 2025. 3

[36] Shuzhe Wang, Vincent Leroy, Yohann Cabon, Boris Chidlovskii, and Jerome Revaud. Dust3r: Geometric 3d vision made easy. In *Proceedings of the IEEE/CVF Conference on Computer Vision and Pattern Recognition*, pages 20697–20709, 2024. 2, 3

[37] Runsen Xu, Weiyao Wang, Hao Tang, Xingyu Chen, Xiaodong Wang, Fu-Jen Chu, Dahua Lin, Matt Feiszli, and Kevin J Liang. Multi-spatialmllm: Multi-frame spatial understanding with multi-modal large language models. *arXiv preprint arXiv:2505.17015*, 2025. 2, 3

[38] Jihai Yang, Shusheng Yang, Anjali W Gupta, Rilyn Han, Li Fei-Fei, and Saining Xie. Thinking in space: How multimodal large language models see, remember, and recall spaces. In *Proceedings of the Computer Vision and Pattern Recognition Conference*, pages 10632–10643, 2025. 2, 3, 7

[39] Chun-Hsiao Yeh, Chenyu Wang, Shengbang Tong, Ta-Ying Cheng, Ruoyu Wang, Tianzhe Chu, Yuexiang Zhai, Yubei Chen, Shenghua Gao, and Yi Ma. Seeing from another perspective: Evaluating multi-view understanding in mllms. *arXiv preprint arXiv:2504.15280*, 2025. 2

[40] Lin Yen-Chen, Pete Florence, Jonathan T Barron, Alberto Rodriguez, Phillip Isola, and Tsung-Yi Lin. inferf: Inverting neural radiance fields for pose estimation. In *2021 IEEE/RSJ International Conference on Intelligent Robots and Systems (IROS)*, pages 1323–1330. IEEE, 2021. 2

[41] Chandan Yeshwanth, Yueh-Cheng Liu, Matthias Nießner, and Angela Dai. Scannet++: A high-fidelity dataset of 3d indoor scenes. In *Proceedings of the IEEE/CVF International Conference on Computer Vision*, pages 12–22, 2023. 4, 5, 6

[42] Kexin Yi, Jiajun Wu, Chuang Gan, Antonio Torralba, Pushmeet Kohli, and Josh Tenenbaum. Neural-symbolic vqa: Disentangling reasoning from vision and language understanding. *Advances in neural information processing systems*, 31, 2018. 3

[43] Kexin Yi, Chuang Gan, Yunzhu Li, Pushmeet Kohli, Jiajun Wu, Antonio Torralba, and Joshua B Tenenbaum. Clevrer: Collision events for video representation and reasoning. *arXiv preprint arXiv:1910.01442*, 2019. 2

[44] Jiahui Zhang, Yurui Chen, Yanpeng Zhou, Yueming Xu, Ze Huang, Jilin Mei, Junhui Chen, Yu-Jie Yuan, Xinyue Cai, Guowei Huang, et al. From flatland to space: Teaching vision-language models to perceive and reason in 3d. *arXiv preprint arXiv:2503.22976*, 2025. 2, 3

[45] Peiyuan Zhang, Kaichen Zhang, Bo Li, Guangtao Zeng, Jingkang Yang, Yuanhan Zhang, Ziyue Wang, Haoran Tan, Chunyuan Li, and Ziwei Liu. Long context transfer from language to vision. *arXiv preprint arXiv:2406.16852*, 2024. 7

[46] Yuanhan Zhang, Bo Li, haotian Liu, Yong jae Lee, Liangke Gui, Di Fu, Jiashi Feng, Ziwei Liu, and Chunyuan Li. Llava-next: A strong zero-shot video understanding model, 2024. 6, 7, 8

[47] Haozhe Zhao, Zefan Cai, Shuzheng Si, Xiaojian Ma, Kaikai An, Liang Chen, Zixuan Liu, Sheng Wang, Wenjuan Han, and Baobao Chang. Mmicl: Empowering vision-language model with multi-modal in-context learning. *arXiv preprint arXiv:2309.07915*, 2023. 2

[48] Hongyan Zhi, Peihao Chen, Junyan Li, Shuailei Ma, Xinyu Sun, Tianhang Xiang, Yinjie Lei, Mingkui Tan, and Chuang Gan. Lscenellm: Enhancing large 3d scene understanding using adaptive visual preferences. In *Proceedings of the Computer Vision and Pattern Recognition Conference*, pages 3761–3771, 2025. 3

[49] Deyao Zhu, Jun Chen, Xiaoqian Shen, Xiang Li, and Mohamed Elhoseiny. Minigpt-4: Enhancing vision-language

understanding with advanced large language models. *arXiv preprint arXiv:2304.10592*, 2023. [2](#), [3](#)

[50] Yiming Zuo, Karhan Kayan, Maggie Wang, Kevin Jeon, Jia Deng, and Thomas L Griffiths. Towards foundation models for 3d vision: How close are we? In *2025 International Conference on 3D Vision (3DV)*, pages 1285–1296. IEEE, 2025. [2](#)

SpatialMosaic: A Multiview VLM Dataset for Partial Visibility

Supplementary Material

A. Statistics of SpatialMosaic-Bench

We provide detailed statistics of *SpatialMosaic-Bench* across different difficulty levels in Fig. 5. Our benchmark contains total 1M QA pairs distributed across six main task categories: Count, Best-View Selection, Existence, Attribute, and Localization. To ensure a comprehensive evaluation of spatial reasoning capabilities, we emphasize challenging scenarios by generating more samples from high and medium difficulty levels. Note that, we enforce that the target object is not visible in the query frame in attribute, existence, and spatial tasks; thus, all QA samples from these tasks fall under the Partially Visible category in the visibility-level distribution.

B. Analysis under Different Conditions

We evaluate SpatialMosaicVLM on *SpatialMosaic-Bench* under varying difficulty levels: Occlusion, Overlap, and Visibility. Performance consistently declines as the difficulty increases, confirming that our categorization accurately captures the challenges of multi-view spatial reasoning. We further compare SpatialMosaicVLM, fine-tuned on our dataset, against InternVL2-8B [6] across all tasks (Fig. 6). **Visibility Level.** For the Object count task, performance drops significantly on the Partially Visible condition, reflecting the inherent difficulty of counting objects that are not fully visible in every frame. For Best-View Selection combined with counting (Bestview count), both Partially and Fully Visible cases show similar moderate performance, as the model must both count instances and identify the optimal frame. Our model substantially outperforms InternVL2-8B on Partially Visible cases across all tasks. **Overlap & Occlusion Level.** For Attribute, Existence, and Spatial Relation tasks, performance degrades from Low to High difficulty levels, with InternVL2-8B showing larger performance drops. This demonstrates that training on *SpatialMosaic* provides improved robustness to such challenging conditions. In contrast, Count and Best-View Selection tasks are not significantly affected by low overlap and occlusion conditions. Instead, their performance is primarily influenced by two factors: the total number of visible instances of the target object category across all frames and the frame-wise distribution of visible instance counts.

C. Technical Details for SpatialMosaic

C.1. Spatial Annotation Framework

The spatial annotation framework establishes the geometric signals used throughout the VQA generation pipeline in *SpatialMosaic-Bench*. In this section, we provide a technical

overview of the annotation process introduced in Sec. 3, focusing on how instance-level visibility, occlusion, and multi-view overlap are computed and stored for later use. We directly reference the definitions in Sec. 3 and clarify how these quantities are applied in the downstream QA-generation stages.

Instance visibility. For each object instance, visibility is determined using the object level occlusion ratio and FoV occlusion ratio defined in Eq. (1) - (5) of Sec. 3.1. Using the ScanNet++ mesh and calibrated camera parameters, each instance’s 3D points are projected into every view, and visibility is computed by rendering both the scene-level depth map and per-instance depth map as described in Eq. (1). FoV truncation is computed via the extended intrinsic formulation in Eq. (3) - (5). These two metrics together form the per-frame visibility profile used in all subsequent stages.

Per-frame visibility masks. Using the visible point sets defined in Eq. (1) and Eq. (4), we construct binary masks for each instance in each frame. These masks define which portion of the 3D geometry is observable and directly ground the multi-view filtering and relation computation.

Overlap computation. Frame overlap is computed using the intersection-over-union of visible 3D point sets as introduced in Eq. (6). This ensures that multi-view sampling captures geometric diversity rather than superficial image similarity. App spatial reasoning tasks (single or multi-category) consume the same visibility and overlap information.

Bounding box transformation. As described in Sec. 3.2, spatial relations are computed by comparing the positions of objects in the viewpoint of the selected query frame. Since the relation is determined by evaluating how the oriented bounding boxes of two instances are ordered along the camera-frame axes, each bounding-box vertex is first transformed into the camera coordinate system of the query view. The transformation is: $v^{(c)} = R_{wc}(v - t_{wc})$ where v is a bounding-box vertex in world coordinates, R_{wc} is the world-to-camera rotation matrix, and t_{wc} is the camera-center translation. The resulting vertices $v^{(c)}$ define the camera-frame bounding boxes used for axis-aligned separation when computing the directional relation in necessary tasks.

C.2. Data Generation Pipeline

The data generation pipeline constructs QA samples by applying task-dependent constraints on the annotated geometric information in appendix Sec. C.1. Once visibility, occlusion, and overlap statistics are available, the pipeline proceeds through the following steps:

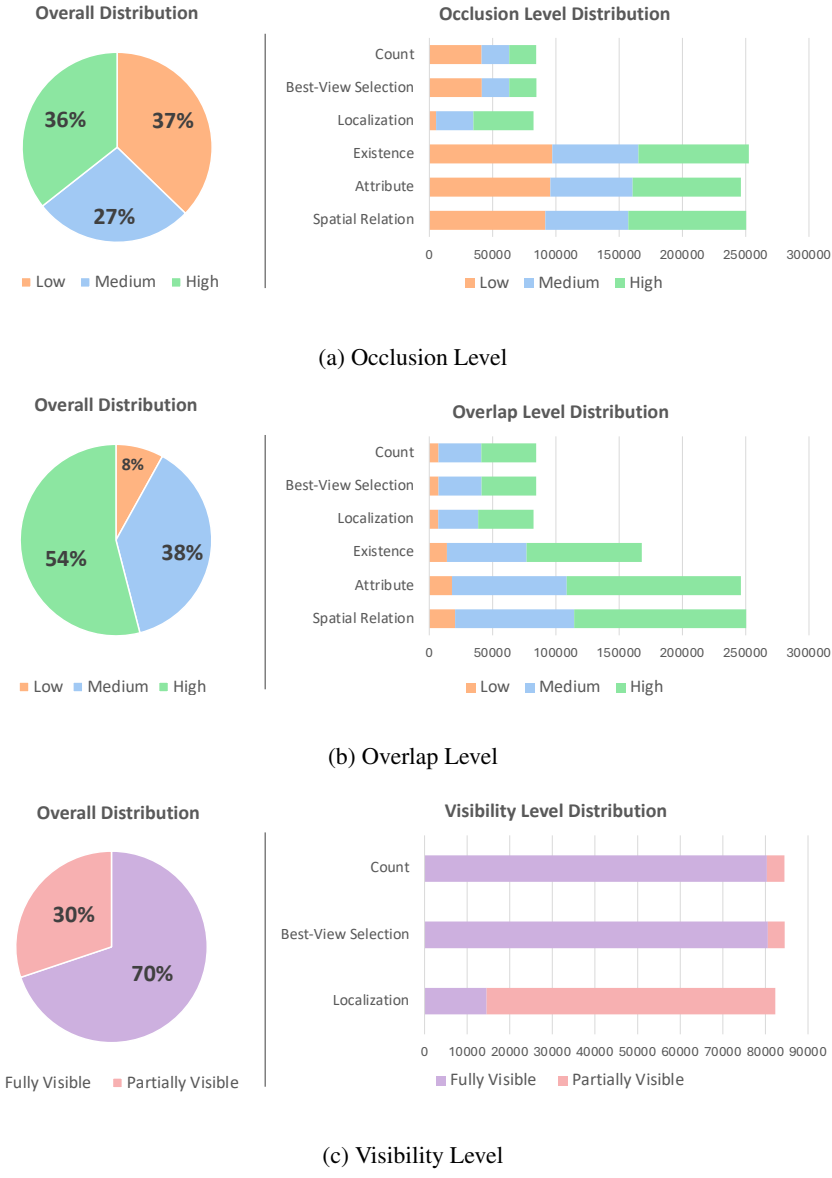


Figure 5. Difficulty Level Distribution

Frame combination construction. For each scene, candidate multi-view combinations are formed by enumerating frame sets that satisfy the required view count and the overlap constraint. Only combinations whose internal view-overlap stays below the specified threshold are retained, ensuring sparse and complementary viewpoints.

Valid instance set collection. Within each retained combination, all object instances that appear in at least one of the included frames are collected. Instances that violate the partial-visibility requirement, such as appearing in every frame or remaining nearly fully occluded across all frames, are removed. The remaining instances carry their semantic

labels, visibility flags, and camera-frame bounding boxes.

Query-frame and object selection. A query frame is selected at random from the valid combination. Depending on the task, the pipeline verifies whether the instances in that frame satisfy the required visibility conditions (e.g., visible source and invisible target pairs for multi-category tasks, or category uniqueness for localization). If the condition is not met, the pipeline attempts another configuration. The task-specific visibility conditions are elaborated in detail in appendix D.

Task-specific geometric computation. Geometric quantities are computed only after a valid configuration is found.

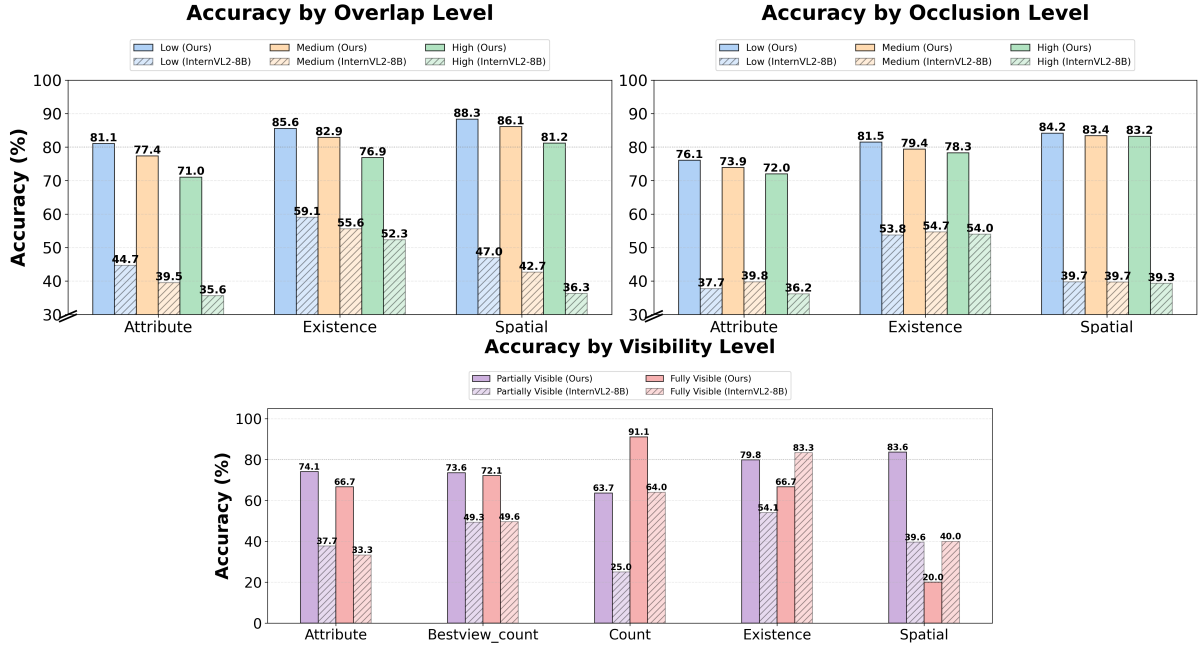


Figure 6. Comparison between SpatialMosaicVLM and InternVL2-8B on *SpatialMosaic-Bench*.

These computations are task-specific, including directional separations between instance bounding boxes, visible-pixel statistics, or merged instance counts across views. All computations operate directly on the pre-annotated camera-frame geometry.

Answer and distractor generation. The computed values are inserted into the task templates. Distractors are generated using the rules defined for each task, such as opposite-direction relations, orthogonal-axis relations, or offset-based count alternatives. All options are de-duplicated, validated, and randomized.

QA assembly. The final QA entry records the selected frame combination, the question constructed from the template with appropriate instances, the multiple-choice options, and all geometric metadata required for evaluation. After such process is completed, a single QA is generated, and the pipeline then moves on to the next sample.

D. SpatialMosaic Task Descriptions

The BaseQAGenerator serves as a foundation for the QA generation process. For each frame in the scene, instance-level occlusion ratios O_s , together with their category labels L_s , are computed as explained in Sec 3.1. Valid frame combinations are first sampled by selecting frame sets that satisfy the per-instance occlusion constraints. These candidate combinations are then filtered using the precomputed overlap table calculated through Eq. (6), such that C_s represents the filtered frame combinations that satisfy both occlusion and

Algorithm 1: BaseQAGenerator

```

1 Input: Scene list  $\mathcal{S}$ , scene-level metadata  $\mathcal{M}$ , frame-level
   metadata  $\mathcal{F}$ 
2 Output: Generated QA set  $\mathcal{Q}$ 
3 Initialization:
4   Build per-scene overlap tables from  $\mathcal{F}$ 
5   Initialize QA buffers and global counters
6 Main loop over scenes:
7 for  $s \in \mathcal{S}$  do
8    $F_s \leftarrow \mathcal{F}[s]$ 
9    $M_s \leftarrow \mathcal{M}[s]$ 
10   $OV_s \leftarrow read\_overlap\_table.\mathcal{F}[s]$ 
11  % Step 1. Occlusion extraction:
12   $(O_s, L_s) \leftarrow extract\_occlusion(F_s)$ 
13  % Step 2. Frame-combination construction:
14   $C_s \leftarrow sample\_valid\_combos(O_s, L_s, s)$ 
15   $C_s \leftarrow overlap\_filtering(C_s, OV_s)$ 
16  % Step 3. Scene-level QA generation:
17  for  $t \in T$  do
18     $G_t \leftarrow get\_qa\_generator(t)$ 
19     $Q_s \leftarrow G_t(s, M_s, F_s, C_s)$ 
20  end
21  % Step 4. Accumulate results:
22   $\mathcal{Q} \leftarrow \mathcal{Q} \cup Q_s$ 
23 end

```

low-overlap conditions. For each task type $t \in T$, a task-specific QA generator G_t produces the corresponding set of QA pairs, Q_s . Finally, all QAs generated for the scene are merged into the global QA set.

Algorithm 2: Object Count (Single-Category)

```

1 Input: scene id  $s$ , per-scene metadata  $M_s$ ,
2 per-scene frame metadata  $F_s$ , Frame combinations  $C_s$ 
3 Output:  $Q_s$ 
4 % Select frame combination from combination sets  $C_s$ 
5 for  $C \in C_s$  do
6   % Step 1. Per-frame visible-instance extraction:
7   for  $f \in C$  do
8     |  $I_c(f) = \text{per\_frame\_instance}(c, f)$ 
9   end
10  % Step 2. Multi-view aggregation:
11   $V_c \leftarrow \bigcup_{f \in C} I_c(f)$ 
12   $GT \leftarrow |V_c|$ 
13  % Step 3. Multiple-choice option generation:
14   $\mathcal{D} \leftarrow \text{count\_distractor}(GT)$   $\mathfrak{D} \leftarrow \{GT\} \cup \text{Sample}_3(D)$ 
15  % Step 4. Output assembly:
16   $Q_s = \text{filling\_qa}(\mathfrak{D}, \mathcal{T}, GT)$ 
17 end

```

Object count. The Object Count task determines how many instances of an object category c are visible throughout the frame combination C . The task first identifies the per-frame visible-instances $I_c(f)$ for all frame combinations, defined as the function $I_c(f) = \{i \mid \text{cat}(i) = c, \text{occ}(i, f) \leq \tau\}$. Multi-view aggregation merges all visible instance sets across the selected frame set, forming the union V_c . The ground-truth count is then obtained as GT , representing the total number of unique instances observed. For answer choice generations, a distractor pool $\mathcal{D} = \{\max(1, GT + \delta) \mid \delta \in \{-3, -2, -1, 1, 2, 3\}\}$ generates incorrect options of a small offset from GT , where three of them are sampled as distractors in \mathfrak{D} . Finally, the *filling-qa* function utilizes all task-specific variables, including the question template \mathcal{T} , to generate the final QA instance as described in Fig. 2.

Best-view selection. The Best-view selection task determines how many instances of an object category c are visible throughout the sampled frames f , and calculates the frame f_b that best depicts the category. The per-frame visible-instance extraction and multi-view aggregation are identical to the object count task. To select the best-view, we first measure how many instances of category c are visible in a frame through $n_c(f)$, then calculate the total visible-pixel area $A_c(f)$ for those instances computed by $\text{vispix}(i, f)$ over all visible instances i in $I_c(f)$. The best frame f_b is determined by the highest visible count; if multiple frames have the same count, ties are broken by visible-pixel comparison. Options \mathfrak{D} contains one correct answer pair with the correct GT and the correct best frame f_b , while three other distractor pairs either have an incorrect count GT' from \mathcal{D} , an incorrect best frame f'_b from $C \setminus \{f^*\}$, or both.

Object localization. The Object Localization task determines whether a target instance i_t is visible in the query

Algorithm 3: Object Bestview (Single-Category)

```

1 Input: scene id  $s$ , per-scene metadata  $M_s$ ,
2 per-scene frame metadata  $F_s$ , Frame combinations  $C_s$ 
3 Output:  $Q_s$ 
4 for  $C \in C_s$  do
5   % Step 1. Per-frame visible-instance extraction:
6   for  $f \in C$  do
7     |  $I_c(f) = \text{per\_frame\_instance}(c, f)$ 
8   end
9   % Step 2. Multi-view aggregation:
10   $V_c \leftarrow \bigcup_{f \in F} I_c(f)$ 
11   $GT \leftarrow |V_c|$ 
12  % Step 3. Best-view selection:
13  for  $f \in C$  do
14    |  $n_c(f) \leftarrow |I_c(f)|$ 
15    |  $A_c(f) \leftarrow \sum_{i \in I_c(f)} \text{vispix}(i, f)$ 
16  end
17   $f_b \leftarrow \arg \max_{f \in F} (n_c(f), A_c(f))$ 
18  % Step 4. Multiple-choice option generation:
19   $\mathfrak{D} = \{(GT, f_b), (GT', f_b), (GT, f'_b), (GT', f'_b)\}$ 
20   $f'_b \leftarrow \text{random\_choice}(C \setminus \{f_b\})$ 
21  % Step 5. Output assembly:
22   $Q_s = \text{filling\_qa}(\mathfrak{D}, \mathcal{T}, GT)$ 
23 end

```

Algorithm 4: Object Localization (Single-Category)

```

1 Input: scene id  $s$ , per-scene metadata  $M_s$ ,
2 per-scene frame metadata  $F_s$ , Frame combinations  $C_s$ 
3 Output:  $Q_s$ 
4 for  $C \in C_s$  do
5   % Step 1. Per-frame visible-instance extraction:
6   for  $f \in C$  do
7     |  $I_c(f) = \text{per\_frame\_instance}(c, f)$ 
8   end
9   % Step 2. Multi-view aggregation:
10   $V_c \leftarrow \bigcup_{f \in F} I_c(f)$ 
11  % Step 3. Localization supervision:
12  if  $i_t$  is visible in  $f_q$  then
13    |  $GT \leftarrow \text{“Yes; } (x_t, y_t)\text{”}$ 
14  end
15  else
16    |  $GT \leftarrow \text{“No”}$ 
17  end
18  % Step 4. Multiple-choice option generation:
19  if  $GT == \text{“Yes; } (x_t, y_t)\text{”}$  then
20    |  $\mathfrak{D} = \{GT, \{\text{Yes; } (x_n, y_n)\}_{n=1}^2, \text{No}\}$ 
21  end
22  else  $GT = \text{“No”}$ 
23    |  $\mathfrak{D} = \{GT, \{\text{Yes; } (x_n, y_n)\}_{n=1}^3\}$ 
24  end
25  % Step 5. Output assembly:
26   $Q_s = \text{filling\_qa}(\mathfrak{D}, \mathcal{T}, GT, f_q)$ 
27 end

```

frame $f_q \in C$, and returns its 2D bounding box center coordinates (x_t, y_t) if it is visible. We construct the GT by determining whether the instance is visible in the query frame using the function $\text{is_visible}(i, f) = 1[\text{occ}(i, f) \leq \tau]$. If the

instance is visible, the GT returns a "Yes" with the instance's 2D bounding box center coordinates (x_t, y_t) , and the distractor options in \mathfrak{D} consist of two positive options with incorrect coordinates $(\{(x_n, y_n)\}_{n=1}^2)$ and a negative option. If the instance is not visible, the GT returns a "No", and the distractor options in \mathfrak{D} consist of three positive options with incorrect coordinates $(\{(x_n, y_n)\}_{n=1}^3)$.

Algorithm 5: Multi-Category Tasks

```

1 Input: scene id  $s$ , per-scene metadata  $M_s$ ,
2 per-scene frame metadata  $F_s$ , Frame combinations  $C_s$ 
3 Output:  $Q_s$ 
4 for  $C \in C_s$  do
5   % Step 1. Per-frame visible-instance extraction:
6   for  $f \in F_s$  do
7      $| I_c(f) = \text{per\_frame\_instance}(i, c, f)$ 
8   end
9   % Step 2. Instance-pair construction:
10  foreach  $\text{combo}(i, C)$  do
11     $| f_q \in C$ 
12     $| (i_s, i_t) \leftarrow \text{select\_src\_tgt\_objects}(f_q)$ 
13  end
14   % Step 3. Spatial-relation evaluation:
15    $R \leftarrow \text{compute\_relation}(i_s, i_t, a)$ 
16   % Step 4. Question formation:
17    $D \leftarrow \text{relation\_distractor}(R)$ 
18    $\mathfrak{D} = \{R, D_1, D_2, D_3\}$ 
19   % Step 5. Output assembly:
20    $Q_s = \text{filling\_qa}(\mathfrak{D}, \mathcal{T}, \mathcal{R}, f_q, i_s, i_t)$ 
21 end

```

Multi-category tasks. Multi-category tasks share the same framework and sampling logic, where their core function is to determine the spatial relation between two object instances. After the initial per-frame visible-instance verification, the pipeline samples source and target instance pairs i_s and i_t from a randomly selected query frame f_q with the following constraints: (1) i_s and i_t cannot be the same object category, (2) the source instance i_s must be visible in the query frame f_q aligned with the predefined visibility threshold, and (3) the target instance i_t must not be visible in the query f_q frame with the same conditions. If all conditions are validated, we obtain an instance pair (i_s, i_t) for spatial inference. Directional relations R are computed by transforming a 3D oriented bounding box into the coordinate system of f_q to analyze their minimum and maximum coordinates along axis a (where $a \in \{x, y, z\}$) for strict geometric assessment.

Although all multi-category tasks share the same process up until computing the spatial relation between the instance pair (i_s, i_t) , the difference arises from constructing distractors D and options \mathfrak{D} :

- **Occlusion-Aware Existence** The occlusion-aware existence task generates a question asking if the target instance exhibits a specific directional relationship from the source

instance (e.g., Is the cup to the right of the wallet?). The corresponding options \mathfrak{D} are binary, containing a "Yes" and a "No", which analyzes the model's capability of determining whether a given relation is true or not. If the relation specified in the question is equal to R from *compute_relation()*, the model chooses "Yes"; otherwise, it chooses "No".

- **Occlusion-Aware Attribute** The occlusion-aware attribute task provides the spatial relation and the source instance, and asks what object depicts the correct spatial relation with the source instance in the query frame f_q (e.g., What object is to the left of the phone?). When constructing the options \mathfrak{D} , we construct an answer pool and a distractor pool: the answer pool contains the correct instance i_t , and the distractor pool contains other instances i_x in the scene that exhibit the opposite relation mentioned in the question by calculating *compute_relation*(i_s, i_x, a). If the computed relation R is the opposite of what is asked in the question, i_x is stored in the distractor pool. In \mathfrak{D} , we sample one option from the answer pool (containing the target instance) and the remaining three from the distractor pool such that there can always be only one correct object that aligns with the requirements in the question.

- **Occlusion-Aware Spatial Relation** The occlusion-aware spatial relation task provides the source instance, target instance, and query frame f_q , and asks what spatial relation the two objects exhibit (e.g., Where is the pillow located in relation to the door?). Upon evaluation on a specific axis a , we first calculate the true spatial relation R between i_s and i_t using *compute_relation()*. The following relation R is the answer for the QA, and is stored in the answer pool. The distractor pool must only consist of spatial relations that do not represent the true relation between i_s and i_t . Therefore, the first distractor D_1 is always the opposite relation of the same axis a of the true relation R . The other two distractors D_2 and D_3 are drawn by calculating the relation of i_s and i_t on the two remaining orthogonal axes b and c . The computed relations R_b and R_c are true relations, so their contradictory relations are added to the distractor pool. For example, if the target instance is "to the left", "below", and "farther" from the source instance, and the evaluation is done on the x axis(left/right), the answer pool will contain "left", while the distractor pool will contain "right", "above", and "closer".

E. Architecture Details of SpatialMosaicVLM

SpatialMosaicVLM constructs a joint representation of a 3D scene by extracting visual tokens and geometric tokens. These tokens are subsequently fused via cross attention to form a unified representation, which serves as input to the language model backbone. Given multi-view images $\{\mathbf{I}_v\}_{v=1}^V$, we employ two encoders: a visual encoder E_{vis} and a geometric encoder E_{geo} .

Visual encoder. We use a pretrained CLIP ViT as the visual encoder. For each view \mathbf{I}_v , the vision encoder produces a sequence of patch-level visual tokens $F_{vis}^{(v)}$:

$$F_{vis}^{(v)} = E_{vis}(\mathbf{I}_v) \in \mathbb{R}^{T_{vis}^{(v)} \times d}, \quad (9)$$

where $T_{vis}^{(v)}$ is the number of visual tokens per view and d is the feature dimension. We aggregate the visual tokens across all views by concatenating them along the token dimension to obtain the global visual token set:

$$F_{vis} = [F_{vis}^{(1)}; F_{vis}^{(2)}; \dots; F_{vis}^{(V)}] \in \mathbb{R}^{T_{vis} \times d}. \quad (10)$$

Geometric encoder. For geometric encoding, we adopt VGGT as E_{geo} , which jointly processes multi-view images to recover scene-level geometric structure. Given the multi-view images, the encoder yields spatial features and camera tokens:

$$(F_{spa}, z) = E_{geo}(\{\mathbf{I}_v\}_{v=1}^V), \quad (11)$$

where $F_{spa} \in \mathbb{R}^{T_{spa} \times d}$ denotes spatial features, and $z \in \mathbb{R}^{V \times d}$ denotes camera tokens. Then, We concatenate spatial features F_{spa} and camera tokens z to obtain the geometric tokens F_{geo} :

$$F_{geo} = [F_{spa}; z] \in \mathbb{R}^{(T_{spa}+V) \times d}. \quad (12)$$

Finally, the visual tokens F_{vis} and geometric tokens F_{geo} are fused through cross attention as described in Sec. 4. The fused representation is then concatenated with the language tokens and fed into the language model backbone for answer generation.

F. Experimental setting

As described in Sec. 3, we construct the SpatialMosaic dataset using ScanNet++ [41], which provides high-quality RGB-D scans along with dense and accurate 3D semantic annotations. For reliable VQA generation, we use only the subset of ScanNet++ scenes that contain dense, high-quality 3D semantic annotations. We select 679 of these annotated scenes for training and 170 for testing. To enable rich and diverse VQA generation, we utilize all annotated object categories present in each scene. Moreover, to ensure that the generated QA pairs cover a wide variety of target–source object combinations, each target object category is explicitly paired with multiple source-object categories. This pairing strategy enables the pipeline to generate a large and diverse set of QA pairs across a wide variety of object pairs. For model training, both VLM-3R and SpatialMosaicVLM are fine-tuned on SpatialMosaic using 8 NVIDIA H200 GPUs with a batch size of 4 for one epoch, which takes approximately 16 hours per model. To conduct evaluation on our *SpatialMosaic-Bench*, we compare with various open-source MLLM baselines, with inference time ranging from 1 to 5

hours depending on model size. Since full-scale comparison experiments are extremely time-intensive even on 8 NVIDIA H200 GPUs, we conduct the fine-tuning and quantitative evaluation in the main paper using a reduced subset of the dataset consisting of 200K training samples and 100K test samples.

G. SpatialMosaic Data Samples

SpatialMosaic dataset provides 12 sub-tasks. We provide the QA examples, as shown in Fig. 7 - 12.

H. SpatialMosaic VQA Templates

We leverage an automated VQA generation pipeline to construct extensive question-answer pairs. The corresponding templates for each task are listed in Table 5.

| Task | Question Template | Answer Type |
|------------------------------------|---------------------------------------------------------------------------------------------------------------------------------------------|--------------------------|
| Object Count | How many {category}(s) are visible across these frames? | {Number} |
| Best View Selection | How many {category}(s) are visible across these frames? And tell me which frame provides the most informative view of the {category}(s). | {Number} + {Frame ID} |
| Existence (LR) | In {frame_id}, is the {object1} {to the left of / to the right of} the {object2} in this viewpoint? | {Yes/No} |
| Existence (AB) | In {frame_id}, is the {object1} {higher than / lower than} the {object2} in this viewpoint? | {Yes/No} |
| Existence (FB) | In {frame_id}, is the {object1} {closer to / farther from} the camera than the {object2} in this viewpoint? | {Yes/No} |
| Attribute (LR) | In {frame_id}, which object appears {to the left of / to the right of} the {object} in this viewpoint? | {Object name} |
| Attribute (AB) | In {frame_id}, which object appears {higher than / lower than} the {object} in this viewpoint? | {Object name} |
| Attribute (FB) | In {frame_id}, which object appears {closer to / farther from} the camera than the {object} in this viewpoint? | {Object name} |
| Spatial Relation (LR / AB / FB) | In {frame_id}, where does the {target} appear in this view relative to the {source}? | {Spatial relation} |
| Localization | Is there a(n) {target} in {frame_id}? If so, what is the bounding box center coordinates? | {Coordinates} |

Table 5. Question templates in **SpatialMosaic** benchmark. LR: Left/Right, AB: Higher/Lower, FB: Closer/Farther.

Task: Object Count



Q) How many *plant pot(s)* are visible across these frames?

A: 4 ✓

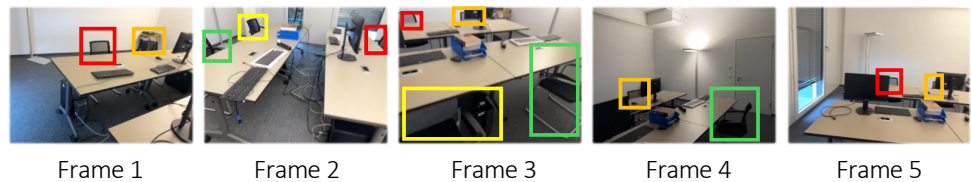
C: 5

B: 2

D: 1

Figure 7. Object Count example

Task: Best-View Selection



Q) How many *chair(s)* are visible across these frames? And tell me which frame provides the most informative view of the chair(s)?

A: 7 chair(s); Frame 3

C: 6 chair(s); Frame 4

B: 4 chair(s); Frame 3 ✓

D: 4 chair(s); Frame 1

Figure 8. Best-View Selection example

Task: Object Localization



Q) Is there a(n) *box* in Frame 4? If so, what is the bounding box center coordinates?

A: Yes; (197,50)

C: Yes; (353,351)

B: No

D: Yes; (127,487) ✓

Figure 9. Object Localization example

Task: Occlusion-Aware Object Existence (left / right)



Frame 1



Frame 2



Frame 3



Frame 4

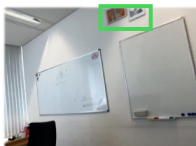
Q) In Frame 1, is the *printer* appears to the right of the *plant* in this viewpoint?

A: Yes ✓

B: No

(a) left / right

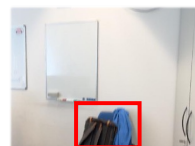
Task: Occlusion-Aware Object Existence (higher / lower)



Frame 1



Frame 2



Frame 3



Frame 4

Q) In Frame 3, is the *picture* appears higher than the *jacket* in this viewpoint?

A: No

B: Yes ✓

(b) higher / lower

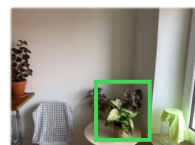
Task: Occlusion-Aware Object Existence (farther / closer)



Frame 1



Frame 2



Frame 3



Frame 4

Q) In Frame 2, is the *plant* appears to the farther from the the camera than the *container* in this viewpoint?

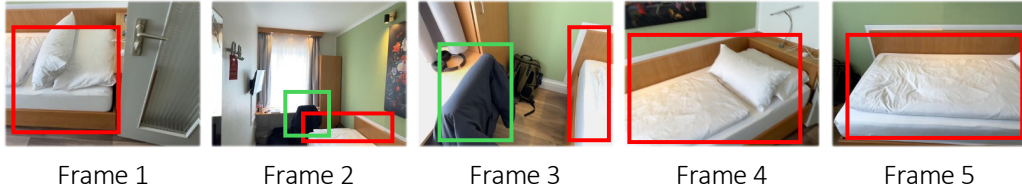
A: No

B: Yes ✓

(c) farther / closer

Figure 10. Occlusion-Aware Object Existence examples

Task: Occlusion-Aware Spatial Attribute (left / right)



Q) In Frame 1, which object appears to the left of the **bed** in this viewpoint?

A: Shower floor
C: Door

B: Jacket ✓
D: Pillow

(a) left / right

Task: Occlusion-Aware Spatial Attribute (higher / lower)



Q) In Frame 5, which object appears higher than the **headphone case** in this viewpoint?

A: Chair
C: White board ✓

B: Heater
D: Table

(b) higher / lower

Task: Occlusion-Aware Attribute (farther / closer)



Q) In Frame 1, which object appears closer to the camera than the **telephone** in this viewpoint?

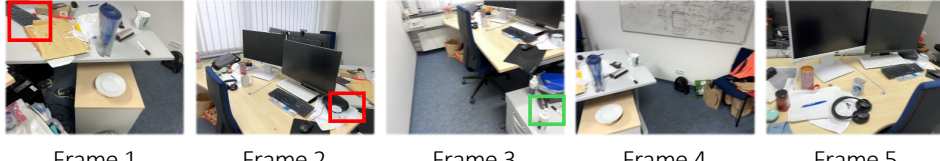
A: A trash bin
C: Power socket

B: Window
D: Bookshelf ✓

(c) farther / closer

Figure 11. Occlusion-Aware Attribute examples

Task: Occlusion-Aware Spatial Relation (left / right)



Frame 1

Frame 2

Frame 3

Frame 4

Frame 5

Q) In Frame 1, where does the *tupperware* appear in this view relative to the *keyboard*?

A: To the right of the keyboard.
B: To the left of the keyboard. ✓
C: Higher than the keyboard.
D: Closer to the camera than the keyboard.

(a) left / right

Task: Occlusion-Aware Spatial Relation (higher / lower)



Frame 1

Frame 2

Frame 3

Frame 4

Q) In Frame 4, where does the *slipper* appear in this view relative to the *thermostat*?

A: Higher than the thermostat.
B: To the right of the thermostat.
C: Lower than the thermostat. ✓
D: Closer to the camera than the thermostat.

(b) higher / lower

Task: Occlusion-Aware Spatial Relation (farther / closer)



Frame 1

Frame 2

Frame 3

Frame 4

Frame 5

Q) In Frame 2, where does the *coffee maker* appear in this view relative to the *sofa chair*?

A: To the left of the sofa chair.
B: Farther from the camera than the sofa chair. ✓
C: Higher than the sofa chair.
D: Closer to the camera than the sofa chair.

(c) farther / closer

Figure 12. Occlusion-Aware Spatial Relation examples